HETE-2 Observations of the X-Ray Flash XRF 040916

Makoto Arimoto,[1] Nobuyuki Kawai,[1] Motoko Suzuki,[3] Rie Sato,[1] Nicolas Vasquez Pazmino,[1]
Takashi Shimokawabe,[1] Takuto Ishimura,[1] Jun'ichi Kotoku,[1] Atsumasa Yoshida,[2] Toru Tamagawa,[3]
Yuji Shirasaki,[3,4] Masaru Matsuoka,[5] Yujin Nakagawa,[2] Nobuyuki Ishikawa,[2] Akina Kobayashi,[2]
Satoshi Sugita,[2] Ichiro Takahashi,[2] Makoto Kuwahara,[3] Makoto Yamauchi,[6] Kunio Takagishi,[6]
Isamu Hatsukade,[6] Jean-Luc Atteia,[7] Alexandre Pelangeon,[7] Roland Vanderspek,[8] Carlo Graziani,[11]
Gregory Prigozhin,[8] Joel Villasenor,[8] J. Garrett Jernigan,[9] Geoffrey B. Crew,[8] Kevin Hurley,[9]
Takanori Sakamoto,[12] George R. Ricker,[8] Stanford E. Woosley,[16] Nat Butler,[8,9] Al Levine,[8]
John P. Doty,[8,10] Timothy Q. Donaghy,[11] Donald Q. Lamb,[11] Edward E. Fenimore,[15] Mark Galassi,[15]
Michel Boer,[13] Jean-Pascal Dezalay,[13] Jean-François Olive,[13] Joao Braga,[17] Ravi Manchanda,[18]
and Graziella Pizzichini[14]

[1]*Department of Physics, Tokyo Institute of Technology, 2-12-1 Ookayama, Meguro-ku, Tokyo 152-8551*
arimoto@hp.phys.titech.ac.jp
[2]*Department of Physics and Mathematics, Aoyama Gakuin University, 5-10-1 Fuchinobe, Sagamihara, Kanagawa 229-8558*
[3]*RIKEN, 2-1 Hirosawa, Wako, Saitama 351-0198*
[4]*National Astronomical Observatory of Japan, Osawa, Mitaka, Tokyo 181-8588*
[5]*JAXA, 2-1-1 Sengen, Tsukuba, Ibaraki 305-8505*
[6]*Faculty of Engineering, Miyazaki University, Gakuen Kibanadai Nishi, Miyazaki, Miyazaki 889-2192*
[7]*LATT, Observatoire Midi-Pyrénées (CNRS-UPS), 14 Avenue E. Belin, 31400 Toulouse, France*
[8]*Center for Space Research, MIT, 77 Vassar Street, Cambridge, MA 02139-4307, USA*
[9]*Space Sciences Laboratory, University of California , Berkeley, CA 94720-7450, USA*
[10]*Noqsi Aerospace, Ltd., 2822 South Nova Road, Pine, CO 80470, USA*
[11]*Deparment of Astronomy and Astrophysics, University of Chicago, 5640 South Ellis Avenue, Chicago, IL 60637, USA*
[12]*Goddard Space Flight Center, NASA, Greenbelt, MA 20771, USA*
[13]*Centre d'Etude Spatiale des Rayonnements, Observatoire, Midi-Pyrénées, 9 Avenue de Colonel Roche, 31028 Toulouse, France*
[14]*INAF/IASF Bologna, Via Gobetti 101, 40129 Bologna, Italy*
[15]*Los Alamos National Laboratory, P.O.Box 1663, Los Alamos, NM 87545, USA*
[16]*Department of Astronomy and Astrophysics, University of California at Santa Cruz,*
477 Clark Kerr Hall, Santa Cruz, CA 95064, USA
[17]*Instituto Nacional de Pesquisas Espaciais, Avenida Dos Astronautas 1758, Saõ Josédos Campos 12227-010, Brazil*
[18]*Department of Astronomy and Astrophysics, Tata Institute of Fundamental Research,*
Homi Bhabha Road, Mumbai, 400-005, India

Abstract

A long X-ray flash was detected and localized by instruments aboard the High Energy Transient Explorer II (HETE-2) at 00:03:30 UT on 2004 September 16. The position was reported to the GRB Coordinates Network (GCN) approximately 2 hours after the burst. This burst consisted of two peaks separated by ~ 200 s, with durations of about 110 s and 60 s. We analyzed the energy spectra of the 1st and 2nd peaks observed with the Wide Field X-Ray Monitor (WXM) and the French Gamma Telescope (FREGATE). We discuss the origin of the 2nd peak in terms of the flux variabilities and timescales. We find that it is most likely to be part of prompt emission, and is explained by a long-acting engine model. This feature is similar to some bright X-ray flares detected in the early afterglow phase of bursts observed by the Swift satellite.

Key words: gamma-rays: bursts — X-rays: bursts — X-rays: individual (XRF 040916)

1. Introduction

X-ray flashes (XRFs) are generally thought to be a sub-class of gamma-ray bursts (GRBs). The main difference between XRFs and GRBs is the energy of the emission; the peak energy, E_{peak}, of XRFs is distributed in the range from a few keV to 10–20 keV, while that of GRBs is distributed from ~ 20 keV to $\sim$ MeV (Barraud et al. 2003). Other properties, such as the timescales or features of the light curve, are similar

for XRFs and GRBs. Using the logarithmic fluence ratio, $\log[S_{\mathrm{X}}/S_{\gamma}]$, to categorize bursts, where S_{X} is the 2–30 keV fluence and S_{γ} is the 30–400 keV fluence, Sakamoto et al. (2005) found that XRFs, X-ray rich GRBs (XRRs), and GRBs form a continuum in the $[S_{\mathrm{X}}, S_{\gamma}]$-plane and in the $[S_{\mathrm{X}}/S_{\gamma}, E_{\mathrm{peak}}]$-plane. This is evidence that all three kinds of bursts are the same phenomenon. Theoretical models that have been proposed to explain these soft events include off-axis viewing (R. Yamazaki et al. 2004), a structured jet (Rossi et al. 2002),

and high-z GRBs (Heise et al. 2001).

In this paper, we report on the detection and localization of XRF 040916 by the HETE-2 satellite (Ricker et al. 2003), and present the results of a detailed temporal and spectral analysis. Since this burst has two peaks within a total time interval of ~ 350 s, we discuss the origin of the long timescale.

2. Observation

2.1. Localization

XRF 040916 triggered the WXM instrument on 2004 September 16, at 00:03:30 UT (GPS: 779328222.72). This burst consisted of two peaks lasting about 110 s and 60 s, separated by a time interval of ~ 200 s. The HETE-2 WXM instrument triggered on the 2nd peak. The initial burst position was based on a rapid ground analysis using the WXM data, and was RA $= 23^{\rm h}01^{\rm m}44^{\rm s}$, Dec $= -5°37'43''$ with a 90% confidence error circle of $18'$ radius. All coordinates given in this paper are J2000.0. This position was reported in a GRB Coordinates Network (GCN) Position Notice at 02:26:16 UT (Y. Yamazaki et al. 2004), and is shown in figure 1. A later, refined ground analysis using the WXM data gave an error box with the following corners: (RA, Dec) = $(23^{\rm h}02^{\rm m}01^{\rm s}68$, $-5°50'09''6)$, $(23^{\rm h}00^{\rm m}23^{\rm s}76$, $-5°37'51''6)$, $(23^{\rm h}00^{\rm m}58^{\rm s}80$, $-5°19'51''6)$, and $(23^{\rm h}02^{\rm m}36^{\rm s}72$, $-5°32'09''6)$ with 90% confidence. This was reported in a GCN Position Notice at 03:58:41 UT (Yamamoto et al. 2004), and is also shown in figure 1. This error box is larger than those usually obtained by HETE-2 because XRF 040916 was faint and the Soft X-ray Camera (SXC; 0.5–10 keV energy band; Villasenor et al. 2003) was not operating at the time. Because no other Interplanetary Network spacecraft observed this burst, the localization could not be refined by triangulation. Identical localizations were
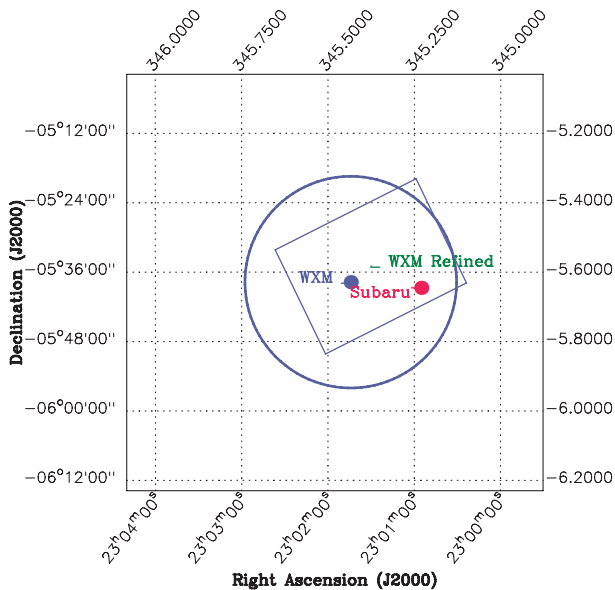
obtained by using the data of the 1st and 2nd peaks separately.

The detection of the optical afterglow was first reported by Kosugi et al. (2004a, 2004b), who found it at RA = $23^{\rm h}00^{\rm m}55^{\rm s}13$, Dec $= -5°38'43''2$ using SuprimeCam on the prime-focus of the Subaru 8.2 m telescope (figure 1). The afterglow was detected in the z', $I_{\rm c}$, $R_{\rm c}$, V, and B-bands in this observation. Henden et al. (2004a, b) also detected it in the $I_{\rm c}$-band with the NOFS 1.0 m telescope. The magnitude of the host galaxy was estimated to be fainter than $R_{\rm c} = 25$, which was the magnitude of the afterglow measured 2 days after the burst. Despite these observations, no redshift has been determined for this event.

2.2. Temporal Properties

Figure 2 shows the light curve of XRF 040916 in six WXM and FREGATE energy bands (2–5, 5–10, 10–17, 17–25, 2–25, and 6–40 keV). There are two peaks in the WXM bands and no significant emission above 17 keV. Table 1 gives the t_{50} and t_{90} durations in the 2–5, 5–10, 10–17, and 6–40 keV energy bands for the first peak, the second peak, and the entire burst.

The 1st peak is composed of two parts: a hard emission region and a soft one, referred to as regions (a) and (b), respectively, in figure 2. This 'hard-to-soft' evolution is typical of GRBs. The duration of the 2nd peak tends to be shorter at higher energies, which is a common feature observed in many GRBs (Link et al. 1993; Fenimore et al. 1995). The duration of the 1st peak in the 10–17 keV band is longer than that in 2–5 keV band because, in the high energy band, the 1st peak consists of two pulses. In region (a) there are few photons in the 2–5 keV band, while there are certain photon contributions in the 5–10 keV and 10–17 keV bands.

2.3. Emission between the 1st and 2nd Peaks

We calculated the count rates before and after the 1st peak, and compared them to the count rate after the 2nd peak. The results show that there is no significant difference between them. We also tried to localize the burst using the photons in the time region between the 1st and 2nd peaks. If there is emission from the burst between the peaks, the resulting localization should be the same as that of the 1st or 2nd peak alone. However, a significant localization could not be obtained, and we conclude that there was no significant emission between the peaks. The corresponding 2σ upper limit is 1.8×10^{-9} erg cm^{-2} s^{-1} (2–400 keV).

2.4. Spectrum

We performed spectral analyses of the two peaks separately, and also of their sum. The background regions used were $-460 \le t \le -330$ s and $-200 \le t \le -70$ s for the 1st peak, and $-110 \le t \le -20$ s and $90 \le t \le 220$ s for the 2nd peak, where t is the time since trigger.

Two types of data sets (*burst data* and *survey data*) are provided by the HETE-2 WXM and FREGATE detectors (Atteia et al. 2003). The burst data are only available when a burst triggers the detector, while the survey data are recorded whenever the HETE-2 satellite is operating. The trigger occurred for the second peak of XRF 040916, and consequently both sets of data were available for it, whereas only the survey data were obtained for the 1st peak.

Fig. 1. HETE-2 WXM localization of XRF 040916. The circle is the initial 90% confidence region and the box is the refined 90% confidence region obtained by ground analysis. The point labeled "Subaru" is the location of the optical afterglow (Kosugi et al. 2004a, b; Henden 2004a, b).
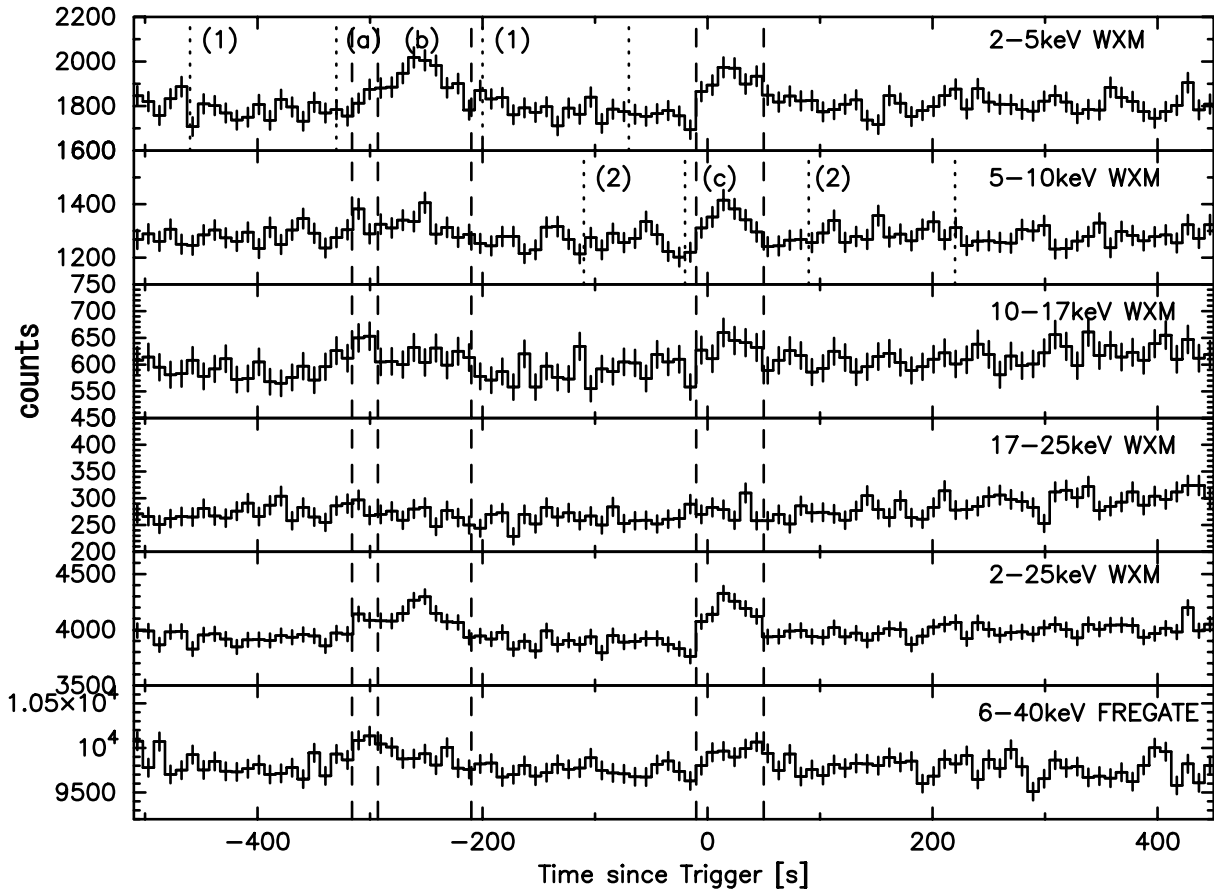
Fig. 2. Light curve of XRF 040916 in six WXM and FREGATE energy bands: 2–5, 5–10, 10–17, 17–25, 2–25, 6–40 keV (top to bottom). The light curve has been binned into 10-second bins. Regions (a) and (b) are the foregrounds of the 1st peak and (c) is the foreground of the 2nd peak. Region (1) represents the background used for the 1st peak and region (2) is the background for the 2nd peak.

Table 1. Temporal properties of XRF 040916.*

Region	1st & 2nd peak		1st peak		2nd peak	
Energy (keV)	t_{90} (s)	t_{50} (s)	t_{90} (s)	t_{50} (s)	t_{90} (s)	t_{50} (s)
WXM						
2–5	374.8 ± 6.2	287.5 ± 3.7	103.3 ± 6.4	39.3 ± 3.2	61.4 ± 4.1	28.3 ± 1.3
5–10	350.2 ± 6.4	292.4 ± 4.1	90.9 ± 1.7	50.4 ± 3.7	39.4 ± 3.4	19.7 ± 2.1
10–17	392.0 ± 17.3	325.6 ± 5.2	120.5 ± 5.2	67.6 ± 4.6	44.3 ± 8.6	18.4 ± 7.2
FREGATE						
6–40	349.0 ± 6.2	109.4 ± 5.4	93.4 ± 13.1	43.0 ± 10.3	55.3 ± 7.6	30.7 ± 9.4

* Quoted errors correspond to 1σ.

The burst data include time-tagged photon data, while the survey data produce time-integrated (4.92 s) data for each wire in the WXM proportional counters. (The WXM instrument is composed of twelve 1-D position-sensitive proportional counters.) In order to improve the signal-to-noise ratio, and consequently the spectral analysis, we applied a cut to the WXM photon time- and energy-tagged data (*TAG data*), using only the photons from the pixels on the six wires of the

X-detector and the two wires of the Y-detector, which were illuminated by the burst. Moreover, because the gain is not uniform at the end of the wires (Shirasaki et al. 2003), we used only the photon counts that registered in the center $\pm$ 50 mm region of the wires. These *optimized* TAG data were extracted and used for the 2nd peak of XRF 040916.

We used the XSPEC v.11.3.0 software package (Arnaud 1996) to perform a spectral analysis. We simultaneously fit the

Table 2. Results of the spectral analyses performed for XRF 040916.*

Region	Function	kT [keV]	α	β	$E_{\mathrm{peak}}^{\mathrm{obs}}$ [keV]	χ^2 (d.o.f.)
1st peak (a)	Blackbody	$5.4^{+1.5}_{-1.2}$				21.68 (21)
	Power law		$-1.6\ ^{+0.2}_{-0.2}$			24.41 (21)
	Power law (above 10 keV)		$-2.0\ ^{+0.3}_{-0.5}$			8.76 (13)
	Cutoff power law		$-0.39^{+0.39}_{-0.95}$		$28.2^{+48.2}_{-10.5}$	19.19 (20)
	Band		$-0.16^{+2.08}_{-1.03}$	$-2.4^{+0.7}_{-7.6}$	$25.6^{+30.9}_{-12.5}$	18.00 (19)
1st peak (b)	Blackbody	$1.2^{+0.3}_{-0.2}$				25.57 (21)
	Power law		$-2.2\ ^{+0.4}_{-0.3}$			18.02 (21)
	Power law (above 10 keV)		$-2.3\ ^{+0.7}_{-1.7}$			13.37 (14)
	Cutoff power law		$-1.9\ ^{+0.7†}_{-...}$		$3.8^{+\ 3.7†}_{-\ ...}$	18.37 (20)
1st peak (a+b)	Blackbody	$2.3^{+0.8}_{-0.6}$				55.60 (34)
	Power law		$-1.8\ ^{+0.1}_{-0.2}$			26.00 (34)
	Power law (above 10 keV)		$-2.0\ ^{+0.3}_{-0.5}$			16.69 (22)
	Cutoff power law		$-1.7\ ^{+0.3}_{-0.2}$		$79.3^{+\infty}_{-59.5}$	25.66 (33)
2nd peak	Blackbody	$2.4\ ^{+0.9}_{-0.8}$				37.80 (17)
	Power law		$-1.9\ ^{+0.2}_{-0.3}$			19.53 (17)
	Power law (above 10 keV)		$-2.5\ ^{+0.6}_{-1.3}$			10.13 (10)
	Cutoff power law		$-1.6\ ^{+0.8}_{-0.5}$		$22.3^{+\infty}_{-18.3}$	18.86 (16)
1st + 2nd	Blackbody	$1.8^{+0.4}_{-0.4}$				82.30 (47)
	Power law		$-1.9\ ^{+0.1}_{-0.2}$			42.16 (47)
	Power law (above 10 keV)		$-2.2\ ^{+0.3}_{-0.5}$			19.45 (28)
	Cutoff power law		$-1.8\ ^{+0.3}_{-0.3}$		$25.8^{+\infty}_{-21.5}$	41.17 (46)

* The quoted errors correspond to 90% confidence.

† The data do not allow a determination of the lower limits for the cutoff power-law function α or $E_{\mathrm{peak}}^{\mathrm{obs}}$ parameters.

WXM and FREGATE data with the four following functions: (1) blackbody function, (2) power-law function, (3) cutoff power-law function, and (4) Band function (Band et al. 1993). Table 2 gives the results of the spectral analysis of each peak.

Although the spectrum is soft, several facts argue against a type I X-ray burst (XRB) as the origin. First, the XRB emission mechanism is blackbody radiation, and we obtained a large χ^2, except for the 1st peak (a), when we used a blackbody model to fit the data. Second, XRBs tend to be found in the galactic plane or globular clusters, and they emit persistent X-rays; the galactic latitude of XRF 040916 is $b = -56°03'$, and there is no known persistent X-ray source or globular cluster at this latitude. Finally, the detection of an optical afterglow for this burst excludes an XRB interpretation.

The analysis of the two peaks separately does not give the best fit. However, considering part (a) of the 1st peak, we obtain a statistically significant improvement using the cutoff power-law or the Band function, compared to the single power-law function, also, the spectrum has a significant break at E_{peak} (table 2). However, in the other regions we could not constrain the parameters by using the Band function.

In the high-energy band (above 10 keV), the photon index, β, tends to be less than -2, and smaller than the photon index, α. $E_{\mathrm{peak}}^{\mathrm{obs}}$ can be constrained to be below 10 keV (where $E_{\mathrm{peak}}^{\mathrm{obs}}$ is E_{peak} in the observer frame). However, the band below 10 keV is near to the low-energy threshold of the

WXM instrument (2 keV). If $E_{\mathrm{peak}}^{\mathrm{obs}}$ is near to the low-energy threshold, the spectrum will appear to follow a power-law, even if it is actually a Band function. We can constrain $E_{\mathrm{peak}}^{\mathrm{obs}}$ using a *constrained* Band function. This can be done both for pure power-law spectra and power-law times exponential spectra with the required curvature in the detector energy range, but only the high-energy part of the Band function is allowed to produce a pure power-law spectrum. This is described in Sakamoto et al (2004). This method is applicable when the spectra of the burst have $E_{\mathrm{peak}}^{\mathrm{obs}}$ near to or below the low-energy threshold of the detector.

Applying the constrained Band function model to each interval of XRF 040916, we obtained a constrained $E_{\mathrm{peak}}^{\mathrm{obs}}$. The results are shown in figure 3 as the posterior probability density distribution for $E_{\mathrm{peak}}^{\mathrm{obs}}$. From these distributions, we find best-fit values for 68%, 95%, and 99.7% probabilities (table 3). We conclude that the spectrum of XRF 040916 is extremely soft compared to that of typical GRBs. $E_{\mathrm{peak}}^{\mathrm{obs}}$ was determined for the 1st peak, but not for the 2nd (it is less than 4.8 keV with 99.7% probability); this hard-to-soft evolution is common in GRBs.

We also calculated the hardness ratio of the 30–400 keV (S_γ) and 2–30 keV (S_X) fluences (table 4). Using this parameter, we can categorize bursts as XRFs when $\log[S_X/S_\gamma] > 0$, X-ray rich GRBs when $-0.5 \le \log[S_X/S_\gamma] \le 0$, and classical hard spectrum GRBs when $\log[S_X/S_\gamma] \le -0.5$. For the 1st peak, as
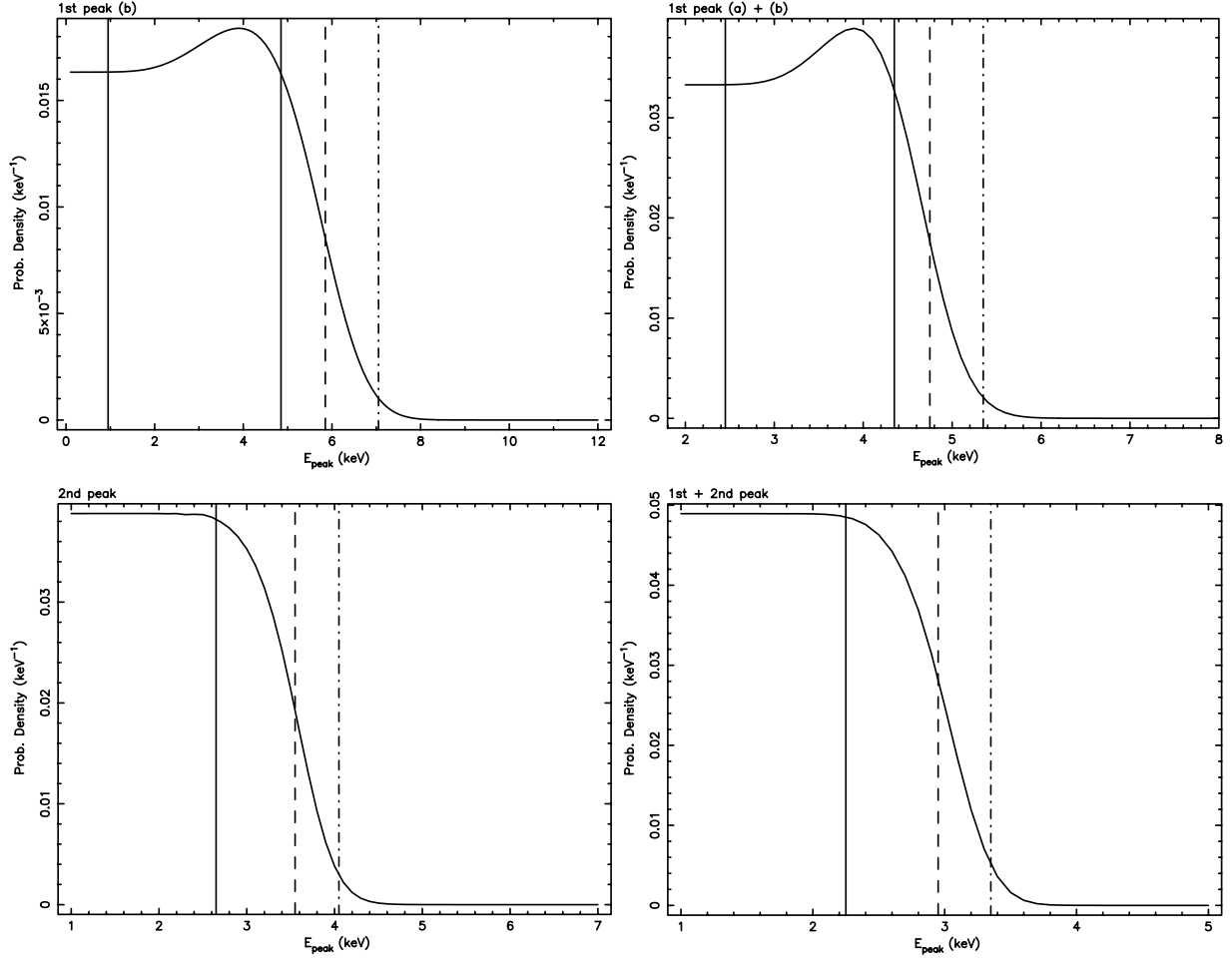
Fig. 3. Posterior probability density distribution for $E_{\rm peak}^{\rm obs}$. The vertical solid lines define the 68% probability interval for $E_{\rm peak}^{\rm obs}$, while the dashed and dotted lines show the 95% and 99.7% probability upper limits on $E_{\rm peak}^{\rm obs}$. Figures from top left to bottom right show the regions for the 1st peak (b), the 1st peak (a) + (b), the 2nd peak, and the 1st + 2nd peaks, respectively.

Table 3. Results of posterior probability density.

Region	Best-fit value (keV)	$E_{\rm peak}^{\rm obs}$ (keV) with 68% prob.	$E_{\rm peak}^{\rm obs}$ (keV) with 95% prob.	$E_{\rm peak}^{\rm obs}$ (keV) with 99.7% prob.
1st peak (b)	3.8	1.0–4.9	< 5.9	< 7.1
1st peak (a) + (b)	3.9	2.5–4.4	< 4.8	< 5.5
2nd peak	...	< 2.7	< 3.6	< 4.2
1st peak + 2nd peak	...	< 2.3	< 3.0	< 3.5

$\log[S_{\rm X}/S_\gamma] \leq 0$ with the cutoff power-law function, this burst would be classified as XRR, rather than an XRF. For the 2nd peak, $\log[S_{\rm X}/S_\gamma]$ is 0.28, with a 90% confidence lower limit of 0.13; that is, the emission of the 2nd peak is softer than that of the 1st peak. Considering finally the total emission of the 1st and the 2nd peaks, the value of $\log[S_{\rm X}/S_\gamma]$, using the cutoff power-law function, is 0.17 with a 90% confidence lower limit of 0.06. Therefore, we regard the entire burst as an XRF.

We consider the 1st peak to be clearly the prompt emission of XRF 040916; we discuss the nature of the 2nd peak in the next section.

3. Discussion

3.1. Redshift Estimates

The spectral softness could be explained if XRF 040916 were a high-redshift GRB. To check this hypothesis, we first estimated the redshift from the Amati relation (Amati et al. 2002) using the 1st peak. Amati et al. (2002) found a relation between the isotropic-equivalent radiated energy, $E_{\rm iso}$, and the burst-averaged value of $E_{\rm peak}$ in the rest frame ($E_{\rm peak}^{\rm rest} \propto E_{\rm iso}^{0.5}$, with $E_{\rm peak}^{\rm rest}$ in keV and $E_{\rm iso}$ in units of 10^{52} erg).

Table 4. Fluences using the cutoff power-law function.

Region	S_X [10^{-7} erg cm^{-2}]	S_γ [10^{-7} erg cm^{-2}]	$\log[S_X/S_\gamma]$ (90% lower limit)
1st peak	4.92±0.72	6.18±0.90	−0.10 (> -0.23)
2nd peak	2.91±0.50	1.53±0.26	0.28 (> 0.13)
1st peak + 2nd peak	7.74±0.91	5.27±0.62	0.17 (> 0.06)
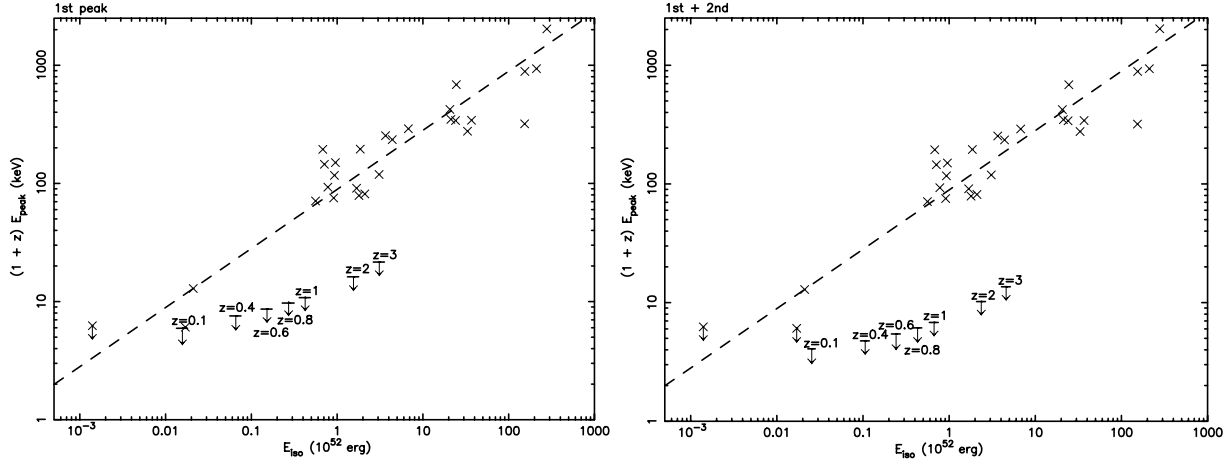
Fig. 4. The (E_{iso}–$E_{\mathrm{peak}}^{\mathrm{rest}}$) -plane where E_{iso} is the isotropic-equivalent radiated energy and $E_{\mathrm{peak}}^{\mathrm{rest}}$ is the peak energy of the νF_ν spectrum, both measured in the rest frame of the burst. The bars are for XRF 040916 at various distances. The crosses: are the BeppoSAX-GRBs (Amati et al. 2002) and HETE-2 GRBs. The dashed line is the equation, $E_{\mathrm{peak}}^{\mathrm{rest}} = 89\, E_{\mathrm{iso}}^{0.5}$ keV, given by Amati et al. (2002). (Left: the 1st peak, right: the entire burst).

Assuming this relation, it is possible to estimate the redshift using only the flux and E_{peak} of a burst. We calculated $E_{\mathrm{peak}}^{\mathrm{rest}}$ and E_{iso} from the spectral parameters of the 1st peak and the entire burst assuming various redshifts. As shown in figure 4, the smaller is the redshift, the more consistent are the computed values with the Amati relation. This result is also consistent with the Subaru redshift constraint of $z < 3$, imposed by its detection of the optical afterglow in the B-band (Kosugi et al. 2004a, b).

We have also computed the upper limit to the pseudo-redshift (with the method described in Pélangeon et al. 2006) using the WXM spectrum for the most intense 15 s long part of the 1st peak. To do this, we derived the upper limit to $E_{\mathrm{peak}}^{\mathrm{obs}}$ using the constrained Band model to fit the data. We find that $E_{\mathrm{peak}}^{\mathrm{obs}} < 6.2$ keV with 90% confidence, leading to a pseudo-redshift of < 0.7, consistent with the preceding results. Thus, we can reject a high redshift for this burst.

3.2. Origin of the 2nd Peak

In the spectral analysis, we could not determine $E_{\mathrm{peak}}^{\mathrm{obs}}$ for the 2nd peak, but we found that above 10 keV the best-fitting model was a power-law, and that $E_{\mathrm{peak}}^{\mathrm{obs}}$ lay in the low-energy region (< 4 keV). Furthermore, the 1st and 2nd peaks are separated by ~ 200 s. This suggests that the 2nd peak could be an X-ray afterglow rather than prompt emission. Indeed, there are at least five possibilities to explain it: (1) beginning of the afterglow, (2) ambient density fluctuations of the X-ray afterglow, (3) patchy shell, (4) refreshed shock, and

(5) long-acting engine model (Ioka et al. 2005). We consider them in the following sections.

3.2.1. Beginning of the afterglow

Piro et al. (2005) said that GRB 011121 and GRB 011211 showed a late X-ray burst taking place a few hundreds of seconds after the prompt emission. The spectral and temporal evolution of the afterglow indicated that fireball evolution took place in the interstellar medium for GRB 011211 and in the wind for GRB 011121, respectively. In both cases, the decay time of a late X-ray burst (i.e., afterglow) is supposed to be proportional to $\sim t^{-1}$ (Sari et al. 1998).

If we set the zero time (t_0) of the emission episode for the 1st peak, then the decay time of the 2nd peak is proportional to $t^{-12.7\pm0.3}$ in the 2–25 keV energy band. Since this result is inconsistent with the above afterglow model, we can reject the possibility of the beginning of the afterglow.

3.2.2. Ambient density fluctuation model

This model explains afterglow variabilities by ambient density fluctuations caused by turbulence in the interstellar medium or variable winds from the progenitor star. If XRF 040916 was in the afterglow stage when the 2nd peak occurred, we can use the following formula for a kinematical upper limit on the variability (Ioka et al. 2005):

$$\frac{\Delta F_\nu}{F_\nu} \leq 2 f_c^{-1} \frac{F}{\nu F_\nu}\left(\frac{\Delta t}{t}\right)^2, \tag{1}$$

where t is the observed time since the burst, F_ν is the assumed power-law baseline of the afterglow flux, F is the bolometric

base flux, $f_c \sim (\nu_m/\nu_c)^{(p-2)/2}$ (where the cooling frequency is ν_c, the characteristic synchrotron frequency is ν_m and the electron power-law distribution index is p), $F/\nu F_\nu \sim (\nu/\nu_c)^{(p-2)/2}$ and Δt, ΔF_ν are the timescale and amplitude deviations above the baseline, respectively. This formula gives the maximum possible afterglow variability due to ambient density fluctuations.

We can estimate the factor $F/(\nu F_\nu)$ assuming the standard afterglow model for $\nu_m < \nu_c < \nu$ (the X-ray band at $t \sim 370$ s). Since $\nu_c \sim 10^{16}$ Hz at t ~ 370 s for $p \sim 2.2$ (Sari et al. 1998), we have $F/(\nu F_\nu) \sim 1$ for the X-ray band ($\nu \sim 10^{19}$ Hz). Furthermore, substituting $\Delta t \sim 60$ s in equation (1), the right-hand side becomes ~ 0.1. But we can clearly see that $\Delta F_\nu/F_\nu \gg 1$ from the flux variabilities in figure 2, because the flux F_ν in the region between the 1st and 2nd peaks ($< 1.8 \times 10^{-9}$ erg cm^{-2} s^{-1} with 2σ confidence level, 2–400 keV), which is assumed to be the afterglow stage, is less than the flux of the 2nd peak (8.3×10^{-9} erg cm^{-2} s^{-1}, 2–400 keV) by a factor of more than 5 with a 2σ confidence level. Since the observed variability exceeds the maximum allowed value, the ambient density fluctuations cannot explain the nature of the 2nd peak.

3.2.3. Patchy shell model

In the patchy shell model the variability timescale of the afterglow at time t must be $\Delta t \geq t$ (Nakar & Oren 2004). In this model, the GRB jet consists of many subjets (R. Yamazaki et al. 2004; Ioka & Nakamura 2001). Since we observe an angular size of γ^{-1} within a GRB jet with a Lorentz factor of γ, the flux depends on the angular structure for the observer. The patchy shell model cannot make a bump with a variability timescale of $\Delta t \sim 60$ s, which is shorter than the observed timescale of $t \sim 370$ s. We can thus marginally reject this model from the point of view of the variability timescale.

In addition, the flux of the 2nd peak is as bright as that of the 1st one. If this burst is explained by the patchy shell model, we must assume a very large shell non-uniformity. In this case, we have to assume that we first observe the dark part of the shell, and then the bright part of the shell as the Lorentz factor drops. As the assumption of a large non-uniformity shell is unrealistic, we can consequently exclude the patchy model.

3.2.4. Refreshed shock model

In this model, multiple shells are ejected at various velocities, and variability occurs when the slow inner shell catches up with the fast outer shell a long time later, since the velocity of the outer shell decreases through interaction with the ambient medium (Rees & Mészáros 1998; Panaitescu et al. 1998; Kumar & Piran 2000; Sari & Mészáros 2000; Zhang & Mészáros 2002). The variability timescale at time t is given by $\Delta t \geq t/4$ (Ioka et al. 2005). In the case of XRF 040916, however, the variability timescale is $\Delta t \leq t/4$ for $t \sim 370$ s and $\Delta t \sim 60$ s, so we can marginally reject the refreshed shock model.

In addition, the flux variability will not be equal to the GRB flux. The relation between the energy increase factor, F, and the flux increase, f, is given by $f = F^{(3+p)/4}$ for $\nu_m < \nu < \nu_c$, and $f = F^{(2+p)/4}$ for $\nu_m, \nu_c < \nu$ (Granot et al. 2003). In either case, $f \sim F$ with typical values of $p \sim 2.2$. Because $f \gg 1$ from the observation, we must have $F \gg 1$. This means that the slow shells have very large energy, which contradicts the

refreshed shock model (refreshed shocks produce changes of less than 1 order of magnitude). Therefore this model, too, can be rejected.

3.2.5. Long-acting engine model

In this model, at the observed time t, the central engine is still active and emitting shells (Rees & Meszaros 2000; Zhang & Meszaros 2002; Dai & Lu 1998). This can explain the variability timescales down to a millisecond, and there is no restriction on the flux variability. The most likely explanation of the 2nd peak is therefore the long-acting engine model. Only this model can explain both the variability timescale and the flux variability for the 2nd peak. In this scenario, both the 1st and 2nd peaks have the same mechanism, and both must show the same spectral and temporal features as GRBs. As we show in subsection 2.2, the timescale of the 2nd peak in table 1 is shorter at higher energies, which is a typical feature of GRBs.

Furthermore, we considered the curvature effect (Kumar & Panaitescu 2000; Liang et al. 2006). This effect occurs when the observer receives the progressively delayed emission from higher latitudes. The following formula represents the curvature effect:

$$F_\nu(t) = A\left(\frac{t - t_0}{t_0}\right)^{-(1+\beta)}, \tag{2}$$

where β is the X-ray photon index during the decay, t_0 is the time zero point of the emission episode related to decay and A is a normalization parameter for the decay component. We applied this effect to the 2nd peak. Because of the poor statistics in the 2nd peak, we used the X-ray photon index ($\beta = 1.9$) during the entire 2nd peak (rise and decay) with the background subtracted in region (2). From a fitting analysis we obtained $t_0 = -34.8 \pm 34.9$ s near to the time zero point for the 2nd peak. This result implies that the zero time for the 1st peak doesn't coincide with the 2nd peak one; the central engine was then reactivated.

Also as shown in subsection 2.4, the spectrum of the 2nd peak is probably softer than that of the 1st. Thus, E_{peak} appears to decrease with time and the flux, in accord with the well-known hard-to-soft evolution in the GRB spectra (Fishman & Meegan 1995). This feature is also consistent with the long-acting engine model, and we consider it to be the most reasonable mechanism to explain the soft 2nd peak of XRF 040916.

Furthermore, we can compare this event with the Swift bursts XRF 050406 and GRB 050502B. Swift (Gehrels et al. 2004) can detect early X-ray afterglows with the X-Ray Telescope (XRT: Burrows et al. 2005a); it has also detected bright X-ray flares 100–1000 seconds after prompt emission for these bursts. They have been explained by the long-acting engine model (Burrows et al. 2005b; Romano et al. 2006, Falcone et al. 2006). Because the XRT is only sensitive to photons in the 0.2–10 keV energy range, the spectral features of the X-ray flares are not as well resolved as those of the prompt emission, and their emission mechanism is still under discussion. In GRB 011211 (Jakobsson et al. 2004; Holland et al. 2002; Piro et al. 2005), GRB 011121 (Piro et al. 2005), and GRB 021004 (Bersier et al. 2003; Halpern et al. 2002), the afterglows included X-ray flares, whose study revealed a wealth of information about the central engine

and its surrounding regions. For XRF 050406, the bright flare occurred ~ 200 s after prompt emission, and for GRB 050502B, it occurred ~ 700 s later . The hard to soft count-rate ratios for the flares were similar to the spectral evolution of the prompt GRB emission. Because the time interval of XRF 040916 is also on the order of ~ 200 s, and the emission of the 1st peak is harder than that of the 2nd according to the $\log[S_X/S_\gamma]$ ratio, the timescale and the spectral evolution between the peaks for XRF 040916 is similar to those of XRF 050406 and GRB 050502B, and can be explained by the long-acting engine model.

4.   Conclusion

In this paper we have reported on HETE-2 WXM/FREGATE observations of XRF 040916, which consists of two peaks separated by ~ 200 s. For this burst, only an upper limit to the redshift has been reported based on optical observations ($z < 3$). Taking into account this limit, our estimate from the Amati relation is consistent with a small redshift. In terms of the spectral evolution, it seems that the 2nd peak is softer than the 1st peak. We studied the emission mechanism of the 2nd peak and sought to find its most probable origin. Considering different models (beginning of the afterglow, ambient density

fluctuation, patchy shell, refreshed shock and long-acting engine model), we found that the long-acting engine model is the most plausible one to explain both the timescale and flux variabilities. In some GRBs or XRFs (e.g. GRB 050502B and XRF 050406), bright X-ray flares were observed; these bursts are also explained by the long-acting engine model (Burrows et al. 2005b). Consequently, our results indicate that the case of XRF 040916 is similar to those of the X-ray flares detected by Swift.

References

Amati, L., et al. 2002, A&A, 390, 81

Arnaud, K. A. 1996, ASP Conf. Ser., 101, 17

Atteia, J.-L., et al. 2003, AIP Conf. Proc. 662, 17

Band, D., et al. 1993, ApJ, 413, 281

Barraud, C., et al. 2003, A&A, 400, 1021

Bersier, D., et al. 2003, ApJ, 584, L43

Burrows, D. N., et al. 2005a, Space Sci. Rev., 120, 165

Burrows, D. N., et al. 2005b, Science, 309, 1833

Dai, Z. G., & Lu, T. 1998, A&A, 333, L87

Falcone, A. D., et al. 2006, ApJ, 641, 1010

Fenimore, E. E., in't Zand, J. J. M., Norris, J. P., Bonnell, J. T., & Nemiroff, R. J. 1995, ApJ, 448, L101

Fishman, G. J., & Meegan, C. A. 1995, ARA&A, 33, 415

Gehrels, N., et al. 2004, ApJ, 611, 1005

Granot, J., Nakar, E., & Piran, T. 2003, Nature, 426, 138

Halpern, J. P., Armstrong, E. K., Espaillat, C. C., & Kemp, J. 2002, GRB Coordinates Network Circ., 1578

Heise, J., in't Zand, J., Kippen, R. M., & Woods, P. M. 2001, in Gamma-ray Bursts in the Afterglow Era, ed. C. F. Costa, F. Frontera, & J. Hjorth (Berlin: Springer), 16

Henden, A. 2004a, GRB Coordinates Network Circ., 2722

Henden, A. 2004b, GRB Coordinates Network Circ., 2727

Holland, S. T., et al. 2002, AJ, 124, 639

Ioka, K., Kobayashi, S., & Zhang, B. 2005, ApJ, 631, 429

Ioka, K., & Nakamura, T. 2001, ApJ, 554, L163

Jakobsson, P., et al. 2004, New Astron., 9, 435

Kosugi, G., Kawai, N., Tajitsu, A., & Furusawa, H. 2004a, GRB Coordinates Network Circ., 2726

Kosugi, G., Kawai, N., Tajitsu, A., & Furusawa, H. 2004b, GRB Coordinates Network Circ., 2730

Kumar, P., & Panaitescu, A. 2000, ApJ, 541, L51

Kumar, P., & Piran, T. 2000, ApJ, 532, 286

Liang, E. W., et al. 2006, ApJ, 646, 351

Link, B., Epstein, R. I., & Priedhorsky, W. C. 1993, ApJ, 408, L81

Nakar, E., & Oren, Y. 2004, ApJ, 602, L97

Panaitescu, A., Meszaros, P., & Rees, M. J. 1998, ApJ, 503, 314

Pélangeon, A., Atteia, J. L., Lamb, D. Q., Ricker, G. R., & The Hete-2 Science Team 2006, AIP Conf. Ser., 836, 149

Piro, L., et al. 2005, ApJ, 623, 314

Rees, M. J., & Mészáros, P. 1998, ApJ, 496, L1

Rees, M. J., & Mészáros, P. 2000, ApJ, 545, L73

Ricker, G. R., et al. 2003, AIP Conf. Proc., 662, 3

Romano, P., et al. 2006, A&A, 450, 59

Rossi, E., Lazzati, D., & Rees, M. J. 2002, MNRAS, 332, 945

Sakamoto, T., et al. 2004, ApJ, 602, 875

Sakamoto, T., et al. 2005, ApJ, 629, 311

Sari, R., & Mészáros, P. 2000, ApJ, 535, L33

Sari, R., Piran, T., & Narayan, R. 1998, ApJ, 497, L17

Shirasaki, Y., et al. 2003, PASJ, 55, 1033

Villasenor, J. N., et al. 2003, AIP Conf. Proc., 662, 33

Yamamoto, Y., et al. 2004, GRB Coordinates Network Circ., 2713

Yamazaki, R., Ioka, K., & Nakamura, T. 2004, ApJ, 607, L103

Yamazaki, T., et al. 2004, GRB Coordinates Network Circ., 2712

Zhang, B., & Mészáros, P. 2002, ApJ, 566, 712